

Statistical analysis of global wind dynamics in vigorous Rayleigh-Bénard convection

K. Petschel,^{1,*} M. Wilczek,² M. Breuer,¹ R. Friedrich,² and U. Hansen¹

¹*Institut für Geophysik, Westfälische Wilhelms-Universität Münster, Germany*

²*Institut für Theoretische Physik, Westfälische Wilhelms-Universität Münster, Germany*

(Received 24 February 2011; published 9 August 2011)

Experimental and numerical studies of thermal convection have shown that sufficiently vigorous convective flows exhibit a large-scale thermal wind component sweeping along small-scale thermal boundary layer instabilities. A characteristic feature of these flows is an intermittent behavior in the form of irregular reversals in the orientation of the large-scale circulation. There have been several attempts toward a better understanding and description of the phenomenon of flow reversals, but so far most of these models are based on a statistical analysis of few-point measurements or on simplified theoretical assumptions. The analysis of long-term data sets ($>5 \times 10^5$ turnover times $\tau_t = d/u_{\text{rms}}$) obtained by numerical simulations of turbulent two-dimensional Rayleigh-Bénard convection allows us to get a more comprehensive view of the spatio-temporal flow behavior. By means of a global statistical analysis of the characteristic spatial modes of the flow we extract information about the stability of dominant large-scale modes as well as the reversal paths in state subspace. We examine probability density functions and drift vector fields of two-dimensional state subspaces spanned by different large-scale spatial modes. This also provides information about the coexistence of dominant modes.

DOI: [10.1103/PhysRevE.84.026309](https://doi.org/10.1103/PhysRevE.84.026309)

PACS number(s): 47.27.te, 47.20.Bp, 47.27.eb, 47.27.ek

I. INTRODUCTION

Even though Rayleigh-Bénard convection, i.e., a buoyancy-driven flow within a fluid layer heated from below and cooled from above, is a classical and intensively studied hydrodynamical problem, it still comprises several open questions (see, e.g., a recent review paper by Ahlers *et al.* [1]).

Experimental (e.g., Refs. [2–4]) and numerical studies (e.g., Refs. [5,6]) of thermal convection have shown that sufficiently vigorous convective flows exhibit a large-scale thermal wind component sweeping along small-scale thermal boundary layer instabilities. A characteristic but still poorly understood feature of these flows is an intermittent behavior in the form of irregular reversals in the orientation of the large-scale circulation (LSC) observed in several experimental [7–9] and numerical studies [10–12]. In three dimensions one has to distinguish two reversal scenarios: The first is characterized by cessation of a partly stable LSC followed by an effective reorganization of the system into a large-scale flow with reversed orientation. The second mechanism results from an azimuthal drift by 180 degrees of the LSC. In this paper we will discuss two-dimensional (2D) convection, so that the only mechanism for a reversal is cessation of the flow structure, and the azimuthal drift will not be addressed further. Such reversals in convecting systems can also be observed in nature. Prominent examples are the reversing geodynamo and reversals in the wind direction of the atmosphere. There have been several attempts toward a better understanding and description of the phenomenon of flow reversals, but so far most of these models are based on statistical analysis of few-point measurements or on simplified theoretical models [13–16]. These models are introduced phenomenologically on the basis of chaotic [13] or stochastic [14–16] ordinary differential equations with two metastable states and are not

based directly on an analysis of the Rayleigh-Bénard flow fields.

In contrast to laboratory studies, direct numerical simulations (DNSs) provide a comprehensive picture of the spatial field structure and are therefore very suitable for examining structural reorganizations within convective flows. The DNS, however, is limited in its spatio-temporal resolution due to computational restrictions.

We were originally motivated by studying convective flows within planetary mantles. Due to the high viscosity of mantle rocks, the value of the Prandtl number given by $\text{Pr} = \nu/\kappa$ (ν, κ denote kinematic viscosity and thermal diffusivity, respectively) is estimated to be around 10^{23} [17]. In this case it is reasonable to consider the infinite Prandtl number limit, implying that mechanical inertia is neglected in the momentum equation. Intrinsically, infinite Prandtl number convection does not contain toroidal motion (horizontal vortices). Schmalzl *et al.* [18] have shown that in this case convection can be reasonably well approximated by a 2D model. This vastly reduces the computational effort of treating such a system numerically and enables us to examine long-term data sets ($>5 \times 10^5$ turnover times $\tau_t = d/u_{\text{rms}}$), being indispensable for a quantitative statistical analysis. Even though mechanical inertia is neglected, i.e., the Reynolds number of the system is zero, convection at a sufficiently high Rayleigh number shows turbulent behavior including intermittent behavior in the form of reversals in the LSC [11]. Most studies examine turbulent Rayleigh-Bénard convection applying rigid boundary conditions, and therefore several phenomena are observed related to viscous boundary layers [19,20]. For example, reversals of LSC are often characterized by the appearance of corner flows, i.e., counterrotating flow structures generated by the viscous boundary layer [21]. Though stress-free boundary conditions are experimentally difficult to realize, they are a good approach for many systems in nature. Many examples can be found in geophysics or astrophysics, such as convection in stars, in the ocean, or in the earth's mantle. In our simulations we investigate

*klaus.petschel@uni-muenster.de

Rayleigh-Bénard convection under stress-free boundary conditions. In such a configuration, viscous boundary layers do not exist, i.e., their thickness is zero.

Assuming the Boussinesq approximation [22], the governing set of nondimensional model equations can be written as

$$\mathbf{0} = -\nabla \tilde{p} + \Delta \mathbf{u} + \text{Ra} T \mathbf{e}_z, \quad (1)$$

$$\nabla \cdot \mathbf{u} = 0, \quad (2)$$

$$\partial_t T + \mathbf{u} \cdot \nabla T = \Delta T, \quad (3)$$

where \mathbf{u} is the velocity vector, \tilde{p} the pressure without the hydrostatic component, T the temperature, and \mathbf{e}_z the unit vector in the z direction. The set of equations constitutes the conservation of momentum, mass, and energy. The equations have been nondimensionalized by means of a characteristic length scale d (the system height), the temperature difference $\Delta T = T_{\text{bot}} - T_{\text{top}}$ between the bottom and the top, and the thermal diffusion time $\tau_\kappa = d^2/\kappa$. In this case the only appearing control parameter is the Rayleigh number $\text{Ra} = \alpha g \Delta T d^3 / \nu \kappa$, specifying the relative strength of buoyancy-driven convection relative to diffusion. Here α denotes the thermal expansion, and g the acceleration of gravity.

Our numerical study aims at a global statistical analysis of high Rayleigh number convection with respect to the stability of dominant spatial modes of LSC as well as characteristic reversal paths.

This paper is organized as follows: First, we will give a short description of the applied numerical method and the considered model parameters in Sec. II. Section III outlines the characteristics of the present LSC and introduces the underlying method of primary mode decomposition applied for the separation of LSC from superimposed plume dynamics. In Sec. IV we use this method to analyze a characteristic path of a reorientation in the LSC by means of a selected reversal sequence. A more global statistical analysis is then given in Sec. V, where we examine probability density functions (PDFs) and drift vector fields of 2D state subspaces spanned by different large-scale modes. This provides information about the coexistence as well as transition paths of dominant large-scale modes. In Sec. VI we address the importance of the large-scale modes and the plume dynamics for the global heat transport followed by a summary of the results (Sec. VII).

II. NUMERICAL MODEL

We use a 2D convection model by Trompert and Hansen [23], based on a finite-volume discretization of the governing equations (1)–(3), at a value of $\text{Ra} = 10^8$ with an aspect ratio of $\Gamma = 2$. Stress-free boundary conditions have been applied on all boundaries. The nondimensional temperatures at the top and bottom are kept constant at zero and one, respectively, whereas the side walls are assumed to be insulating. As initial condition we have chosen the conductive state, with a superimposed high-frequency random perturbation to inhibit an induced particular evolution. The grid resolution is $N_x = 256$ grid points in the horizontal direction and $N_z = 128$ in the vertical direction. Thermal convection at high Rayleigh numbers is characterized by the appearance of thin thermal boundary layers at the top and bottom walls, which have to be appropriately resolved. Therefore, we use a grid refinement in

the vertical direction toward the top and bottom walls defined by roots of Chebyshev polynomials [24]. In our case, at least 10 grid points are then lying within the thermal boundary layer region.

III. LARGE-SCALE CIRCULATION AND PRIMARY MODE DECOMPOSITION

The convective flow of our long-term simulation at $\text{Ra} = 10^8$ and aspect ratio $\Gamma = 2$ features a developed LSC superimposed by small-scale boundary layer instabilities in the form of thin plumelike up and down wellings. These boundary layer instabilities are irregular, disconnected structures carried by the thermal wind. The LSC turns out to be only temporarily stable by switching predominantly between clockwise or anti-clockwise orientated one- and two-cell patterns, respectively. Breuer and Hansen [11] showed for similar model parameters that there exist four metastable states that turned out to be stationary solutions of the governing equations (1)–(3). These fixed-point solutions represent the primary large-scale flow pattern as described above. The temporal flow structure can now be interpreted by different primary modes superimposed by plumes that act in a sense as noise. To analyze the large-scale dynamics, i.e., flow reversals and primary mode selection, it is reasonable to separate the large-scale wind pattern from the small-scale plume dynamics. In more complex geometry (as e.g., Ref [25]; three-dimensional cylindrical coordinates) methods such as proper orthogonal decomposition [26] can be used to determine an orthonormal system. However, for our current study of the 2D system, an expansion in eigenfunctions of the Laplacian $\Delta \mathbf{u}$ in the momentum equation (1) is a convenient way to characterize the stationary solutions of the velocity field qualitatively. This can be expressed by

$$\mathbf{u}(x, z, t) = \sum_m \sum_l \xi_{ml}(t) \hat{\mathbf{u}}_{ml}(x, z)$$

with 2D orthonormal eigenfunctions $\hat{\mathbf{u}}_{ml}$ and corresponding time-dependent amplitudes ξ_{ml} . The eigenfunctions can be separated into a vertical and a horizontal component given by

$$\hat{\mathbf{u}}_{ml}(x, z) \cdot \mathbf{e}_x = \sqrt{2} \sin\left(m\pi \frac{x}{x_{\text{max}}}\right) \cos\left(l\pi \frac{z}{z_{\text{max}}}\right),$$

$$\hat{\mathbf{u}}_{ml}(x, z) \cdot \mathbf{e}_z = \sqrt{2} \cos\left(m\pi \frac{x}{x_{\text{max}}}\right) \sin\left(l\pi \frac{z}{z_{\text{max}}}\right),$$

where x_{max} and z_{max} are the length and height of the simulation domain. The eigenfunctions $\hat{\mathbf{u}}_{ml}$ satisfy the applied stress-free boundary conditions. Based on the two-dimensionality and the incompressibility equation (2), the vertical and horizontal component of the velocity are directly coupled as both velocity components can be derived from a stream function. Thus it suffices to examine one component. Due to orthonormality of the eigenfunctions, projection of the vertical velocity component u_z gives the amplitude corresponding to the mode m, l , defined by

$$\xi_{ml}(t) = \int_0^{x_{\text{max}}} \int_0^{z_{\text{max}}} u_z(x, z, t) (\hat{\mathbf{u}}_{ml}(x, z) \cdot \mathbf{e}_z) dx dz.$$

As described above, the applied functions for primary mode projection are eigenfunctions of the Laplacian $\Delta \mathbf{u}$ but not of

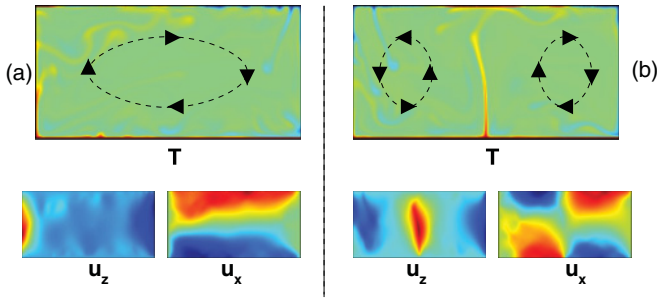


FIG. 1. (Color online) Snapshots of the flow structure for two different representative states of LSC. Shown are visualizations of temperature T and velocity components u_x, u_z for (a) a one-cell and (b) a two-cell LSC, respectively. The plots are color coded: For the temperature field, red and blue indicate hot and cold material, and for the velocity components, red and blue indicate positive and negative values.

the full nonlinear system given by Eqs. (1)–(3). Therefore they are independent of the Rayleigh number and do not resolve boundary layers and plume dynamics. However, the primary modes shown in Fig. 2 represent to first order the large-scale dynamics (Fig. 1). For example, the large-scale dynamics of the flow showing a one-cell LSC state [Fig. 1(a)] can approximately be represented by the \hat{u}_{11} mode [Fig. 2(a)]. An appropriate superposition of odd modes, where the velocity cancels out in the bulk but adds up in the bound, leads to a LSC state with thinner velocity boundary layers. Hence this approach will be used to separate the LSC from the plume dynamics.

IV. REVERSAL SEQUENCE AND REPRODUCTION OF THE VERTICAL VELOCITY

As stated above, a characteristic feature of high Rayleigh number convection appears to be a frequent reorientation of the LSC. This is illustrated in Fig. 3 showing the temporal evolution of the vertical velocity at two distinct measurement points, located at middepth at the left and the right side walls, respectively. One can clearly see the temporal correlation of these two measurements reflecting the large-scale dynamics of the system. A change in sign in both measurements at the side walls indicates a global reorientation of the LSC, also termed flow reversal. Concerning this matter, the prominent question is: What triggers such a reversal, and what are the characteristics of a reversal path?

In the following we will discuss exemplarily the flow evolution path during one arbitrarily selected reversal. To

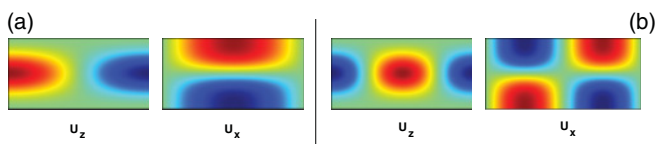


FIG. 2. (Color online) Vertical and horizontal eigenfunction components of a single-cell pattern \hat{u}_{11} (a) and a two-cell pattern \hat{u}_{21} (b). The plots are color coded, where red and blue indicate positive and negative velocities, respectively.

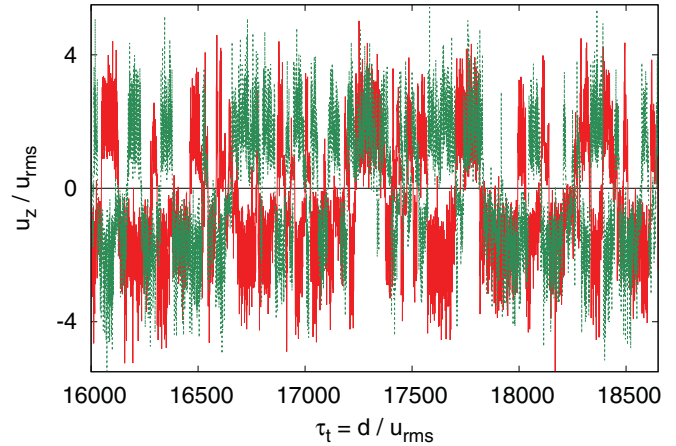


FIG. 3. (Color online) Temporal evolution of the vertical velocity at the side walls (solid red line [left] and dashed green line [right]) at middepth indicating reversals in the orientation of the LSC. If the velocity components have different signs, the system must be organized into an odd number of convection cells, and if the signs are the same, the flow is organized into an even number of convection cells.

this end different stages of the temporal evolution of one representative reversal are displayed in Fig. 4. Initially a stable one-cell structure has formed, which leads to a high amplitude ξ_{11} [Fig. 4(a)] acting as an indicator for a superposition of odd modes. This pattern is superimposed by small-scale plumes that contribute to eigenfunctions of higher orders. Due to the strong boundary layer dynamics, a few strong plumes develop from time to time. If such a plume rises fast enough to disturb the flow structure, the current flow pattern becomes unstable. After a short period of plume-dominated behavior, a two-cell pattern evolves with respect to the global wind [Fig. 4(b)]. In terms of the amplitudes this means that there is a strong ξ_{21} and vanishing ξ_{11} . This relatively stable flow pattern with two equally sized cells changes its structure after a few circulation periods by varying the size of both convection cells. This time-dependent structure becomes unstable evolving toward a three-cell pattern with one big cell in the middle and two small cells at each side of the main cell. With increasing time, the flow librates between a one- and two-cell pattern of different cell size. The amplitudes ξ_{11} and ξ_{21} are reflecting this behavior in strong alternating fluctuations, where it is possible that both amplitudes are nonzero [Fig. 4(c)]. Later the flow has established again a stable one-cell state but in a reversed direction and with zero ξ_{21} [Fig. 4(d)]. In our simulations such a generic reversal path is the most frequent evolution of change in flow orientation. However, it is not necessary that a breakdown of a stable one-cell state always leads to a reversal of flow direction. It is just as likely for the flow to establish an LSC in the same direction as before.

The temporal evolution of the vertical velocity at the side walls at middepth can be expanded in a series of eigenmodes as discussed in the theoretical section. For an adequate analysis of primary mode decomposition it is interesting to see how many modes are sufficient to describe the dynamics of the system. Figure 5 displays the comparison between the

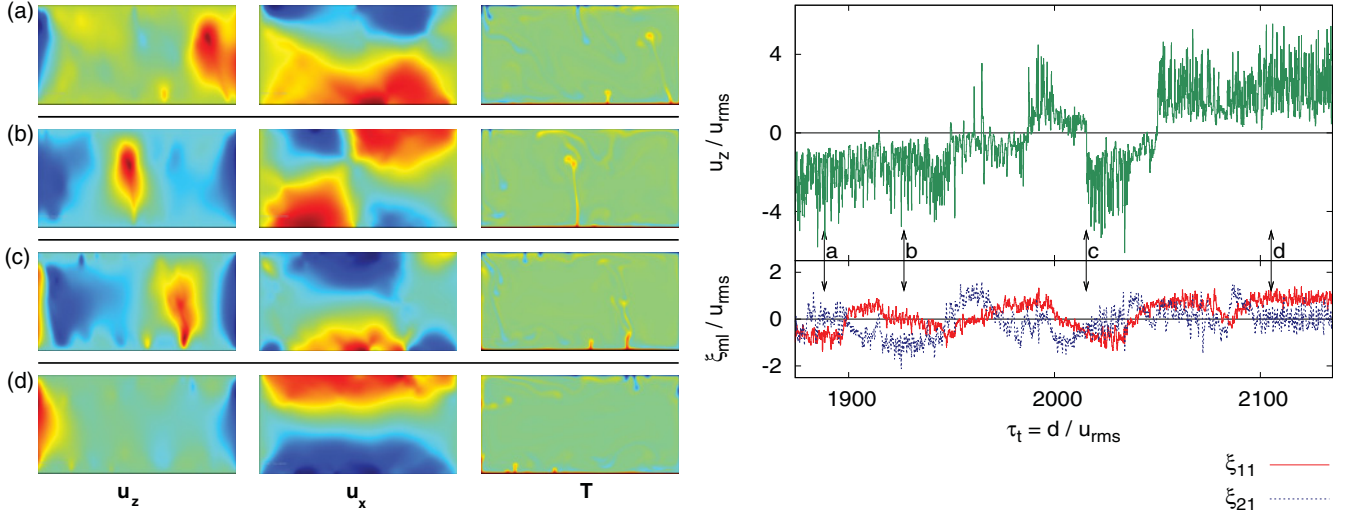


FIG. 4. (Color online) (Left panels) Snapshots of the flow structure at distinct points in time. Shown are snapshots of the vertical velocity component u_z (left), the horizontal velocity component u_x (middle), and the temperature field (right). (Right panel) Temporal evolution of the vertical velocity (green (upper) line) at the left side wall at middepth and the corresponding evolution of the modes ξ_{11} (solid red) and ξ_{21} (dashed blue). The temporal evolution indicates a reversal of sign of a single-cell pattern. The arrows with letters a–d mark the distinct states seen in the left panel.

temporal evolution of the vertical velocity at the side walls at middepth and a reduced model of a finite set of modes:

$$\mathbf{u}(x, z, t) = \sum_{m=1}^N \xi_{m1}(t) \hat{\mathbf{u}}_{m1}(x, z) \quad \text{for } N \leq 5.$$

For a decreasing number of participating modes the amplitude of the vertical velocity component is decreased, but the correlation remains robust for all $N > 1$. Hence the global dynamics of the system as well as the reversal behavior

can be represented by only the first two modes, ξ_{11} and ξ_{21} . This means that the first two modes act as the leading modes in a superposition. However, if more modes are incorporated, there is a better agreement of the amplitudes.

V. PDFS AND DRIFT VECTOR FIELDS OF 2D STATE SUBSPACES

In the previous section we discussed exemplarily one reversal path. We showed that in this specific case the change from a one-cell LSC to a one-cell circulation with reversed orientation is not a direct transition but follows a path over a dominant two-cell state. To answer the question if this is a characteristic behavior, it is insightful to examine the 2D PDF of the amplitudes of the dominant modes ξ_{11} and ξ_{21} . This PDF of the 2D subspace allows us to extract the statistical dependency with respect to these two primary large-scale modes. However, due to the restriction of dimension in state subspace we cannot extract information of the other modes at the same time. This means that this projection allows us only to discuss the dependency of two modes on each other. To study the dynamics of transitions between the two states, we estimate finite-time drift vector fields of different pairs of amplitudes. Similar as in the theory of stochastic processes [27], these may be defined as

$$\mathbf{D}(\tilde{\mathbf{q}}) = \frac{1}{\tau} \langle \mathbf{q}(t + \tau) - \mathbf{q}(t) \mid \mathbf{q}(t) = \tilde{\mathbf{q}} \rangle,$$

where $\mathbf{q}(t) = [\xi_{m1}(t), \xi_{nk}(t)]$ is the position in the state subspace and τ is taken much smaller than the average difference between two reversals τ_r . We have checked that the topological structure of the vector field is robust as long as the condition $\tau \ll \tau_r$ holds. The interpretation of this quantity is particularly intuitive; given a certain pair of values (ξ_{m1}, ξ_{nk}) in state subspace, the drift vector field indicates the direction of the temporal evolution of these two amplitudes on the

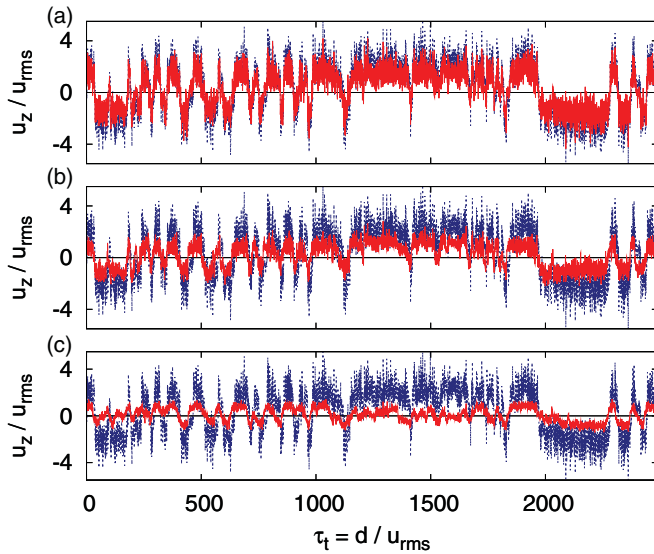


FIG. 5. (Color online) Temporal evolution of the vertical velocity component u_z (dashed blue) and of a reduced model (solid red), which contains only a few basic modes. (a) ξ_{11} to ξ_{51} , (b) ξ_{11} and ξ_{21} , and (c) ξ_{11} . For decreasing N the amplitude of the reproduced vertical velocity component is decreasing, but even the $N = 2$ case strongly correlates with the full data set.

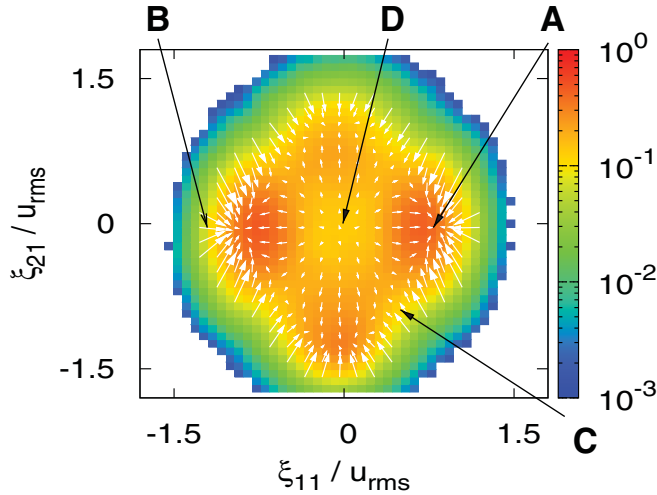


FIG. 6. (Color online) PDF and drift vector field for the 2D state subspace spanned by the primary modes ξ_{11} and ξ_{21} . An unstable fixed point in the center as well as four attractive fixed points in the limit points are clearly visible. The PDF indicates that both modes do not appear simultaneously.

statistical average. Hence this quantity allows us to determine if a typical reversal path comprises a spontaneous switching of the direction of the LSC or if higher-order modes are involved.

The PDF extracted from the primary modes ξ_{11} and ξ_{21} in Fig. 6 corresponding to the one- and two-cell flow pattern shows four isolated maxima indicating the most probable configurations, two distinct maxima with respect to the one-cell circulation with zero ξ_{21} , and two distinct maxima of the two-cell circulation with zero ξ_{11} . This indicates that both flow structures do not occur simultaneously. Additionally the orientation of the drift vector field marked with the white arrows reveals the statistical motion in the state subspace. There are four stable fixed points that correspond to the maxima of the PDF. Due to an unstable fixed point the system is pushed away from the origin; this implies that a reversal in the orientation of one of these modes always goes along with the appearance of the second dominant mode and vice versa. The absolute value of the vector field implies how strong the system is attracted into the fixed-point solution. Due to this absolute value in combination with the higher probability of ξ_{11} it is clear that the one-cell circulation is the most dominant flow pattern. Of course, it is also interesting to study relations involving higher-order modes. Different state subspaces of higher-order modes are shown in Fig. 7. Contrary to the ξ_{11}, ξ_{21} subspace the amplitudes ξ_{11} and ξ_{31} are not independent of each other, as Fig. 7(a) reveals. Both amplitudes in this state subspace are nonzero at the most probable configuration, which indicates that the one- and three-cell pattern exist simultaneously. This also indicates that a one-cell LSC structure not only consists of one mode but of the superposition of odd modes. However, ξ_{11} is the strongest amplitude. The drift vector field indicates two stable attractors that conform with the most probable configurations, which are not subdivided into distinct maxima. In the origin the drift vector field specifies a saddle point that corresponds to the appearance of other modes. Similar to the one- and three-cell

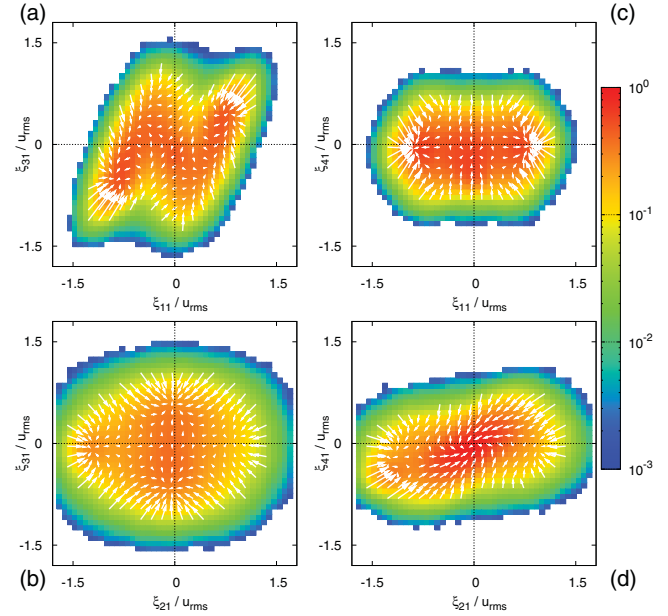


FIG. 7. (Color online) PDF and drift vector field extracted from the 2D state subspace spanned by different modes ξ_{ml} . The most probable configurations (except from both modes vanishing simultaneously) in (a) and (d) are located at a position in subspace where both amplitudes are nonvanishing, which indicates that both modes appear simultaneously, so that $\hat{\mathbf{u}}_{31}$ is coupled to $\hat{\mathbf{u}}_{11}$ and $\hat{\mathbf{u}}_{41}$ is coupled to $\hat{\mathbf{u}}_{21}$ whereas the modes in (b) and (c) are uncoupled and do not appear simultaneously.

pattern, Fig. 7(d) reveals a coexistence of the two- and four-cell flow structures. However, there is no coexistence between the mode amplitudes in Figs. 7(b) and 7(c). This implies that there is only a connection between the one- and three-cell and the two- and four-cell flow circulations, i.e., between odd and even modes.

VI. PLUME DYNAMICS AND HEAT TRANSPORT

Due to the analysis of the state subspace we are able to describe the flow phenomena in terms of amplitudes extracted from spatial modes. In order to extract more information about the flow structures in the ξ_{11}, ξ_{21} subspace (Fig. 6), typical flow fields belonging to different points in the ξ_{11}, ξ_{21} plane are displayed in Fig. 8. This establishes a connection between different points in state subspace and the corresponding flow configurations and allows us to discuss the statistical results with respect to dynamical features of the flow. At the distinct maxima, indicating the most probable configuration with respect to the one-cell pattern, a flow circulation with only a few plumelike structures has developed [Fig. 8(a)]. At this stage the plumes do not reach far into the bulk. The thermal instabilities travel along the boundary layer and do not grow until they cross approximately two-thirds of the simulation domain. With increasing ξ_{11} the flow gets more nonstationary. The plumes separate earlier from the boundary layer and interact with the bulk more frequently [Fig. 8(b)]. Both velocity components in Figs. 8(a) and 8(b) indicate that one circulation cell covers the whole simulation domain. During the transition between a one- and two-cell structure both amplitudes are nonvanishing, and hence the flow is a superposition of a

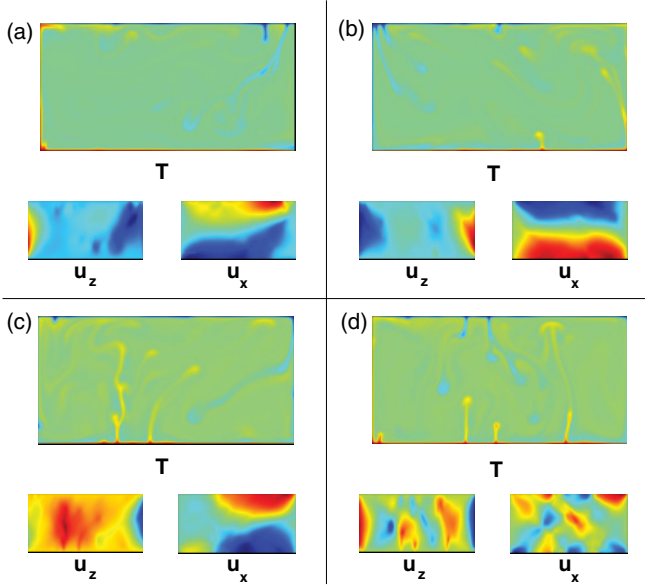


FIG. 8. (Color online) Snapshots of the flow structure at distinct points in state subspace spanned by ξ_{11} and ξ_{21} [see Figs. 6(a)–(d)]. Shown are snapshots of the temperature field (top), the vertical velocity component u_z (bottom left), and the horizontal velocity component u_x (bottom right).

one- and a two-cell pattern. Such a flow pattern with one big and one small convection cell is displayed in Fig. 8(c). Due to a high magnitude of the drift vector field there is a strong variation in the flow structure. Similar to Fig. 8(b) these variations are related to an increased plume activity. This points out that the high magnitude of the drift vector field is linked to a strong interaction of the plumes with the flow. Hence, a transition between two fixed points always goes along with the development of a strong plume, which perturbs the stable flow pattern. In the case where both dominant modes ξ_{11} and ξ_{21} are equal to zero, the flow has to organize in higher-order modes. The plume-dominated dynamics is strongly time dependent with no global predominant pattern [Fig. 8(d)]. The velocity components u_x and u_z at this point in state subspace display a spatially uncorrelated picture without predominant flow structure. The irregularly distributed flow is unstable in time and tries to reorganize into a structure of large-scale thermal circulation. The typical flow fields displayed in Fig. 8 indicate that pure one- and two-cell flow structures occur only at the fixed points of the drift vector field in state subspace (Fig. 6). Outside of these fixed points the flow is characterized by higher-order flow structures, a superposition of different flow patterns [Fig. 8(c)], and in particular by an increased plume activity. Hence, there is no clear one- or two-cell structure outside of the fixed points, without interaction of plumes with the bulk.

With respect to the phenomena of large-scale circulation, as discussed above, the heat transport is of special interest. The Nusselt number measures the ratio of actual heat flux due to advection q_{adv} and conduction q_{cond} to the heat flux of the purely conductive state q_0 and is given by

$$\text{Nu} = \frac{q_{\text{adv}} + q_{\text{cond}}}{q_0}.$$

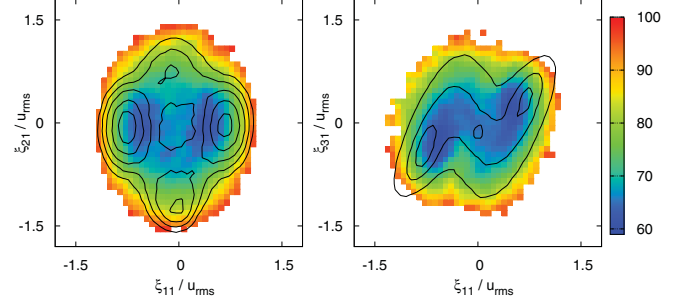


FIG. 9. (Color online) Temporal average of the Nusselt number conditioned on the one- and two-cell pattern, given by $\langle \text{Nu} | \xi_{11}, \xi_{21} \rangle$ (left) and on the one- and three-cell pattern, given by $\langle \text{Nu} | \xi_{11}, \xi_{31} \rangle$ (right). The contour map shows the PDF from the 2D state subspace [see Figs. 6 and 7(a)].

The spatially averaged Nusselt number can be written as

$$\text{Nu}(t) = \left\langle \langle u_z(x, z, t) T(x, z, t) \rangle_x - \frac{\partial}{\partial z} \langle T(x, z, t) \rangle_x \right\rangle_z.$$

A possible connection between global dynamics and the Nusselt number has been suggested previously by a number of authors [1, 6, 28]. Several experiments indicate that the Nusselt number is insensitive to changes in the large-scale dynamics. However, there are several numerical studies [29, 30] and theoretical hints [31] indicating a sensitivity to changes assuming stress-free boundary conditions. Through our analysis we can combine generic flow structures with coordinates in state subspace. To provide information about the heat transport of dominant modes, we analyze the 2D temporal average of the Nusselt number conditionally averaged with respect to position in the state subspace of the amplitudes $\xi_{m1}(t)$ and $\xi_{n1}(t)$, given by $\langle \text{Nu}(t) | \xi_{m1}(t), \xi_{n1}(t) \rangle_t$. This quantity in combination with the flow examples of Fig. 8 reveals how effective the different flow structures are for cooling and heating. The temporal average of the Nusselt number conditionally averaged with respect to the one- and two-cell pattern (Fig. 9) increases for increasing amplitudes. This implies that for plume-dominated flow structures, where the instabilities interact frequently with the bulk, the Nusselt number is much higher. For the zero two-cell pattern domain there are two minima in the Nusselt number visible. For this domain in state subspace, the plumes do not reach far into the bulk, as seen in Fig. 8(a). The increased Nusselt number at high amplitudes, i.e., high magnitudes of the drift vector field, and the minima in the Nusselt number near the fixed points of the drift vector field point out the plumes that interact with the bulk increase the heat transport.

To extract further information about the Nusselt number with respect to the primary modes, we examine the PDF of the Nusselt number conditionally averaged with respect to the most probable configuration in state subspace. For this quantity we select a domain around the maxima of the PDF with respect to a threshold. The PDF of the Nusselt number conditionally averaged with respect to the isolated maximum of the clockwise and anticlockwise orientated one-cell circulation is displayed in Fig. 10. By varying the threshold, more or fewer fluctuations in the form of plumes influence the PDF. Instead of a Gaussian distribution, the

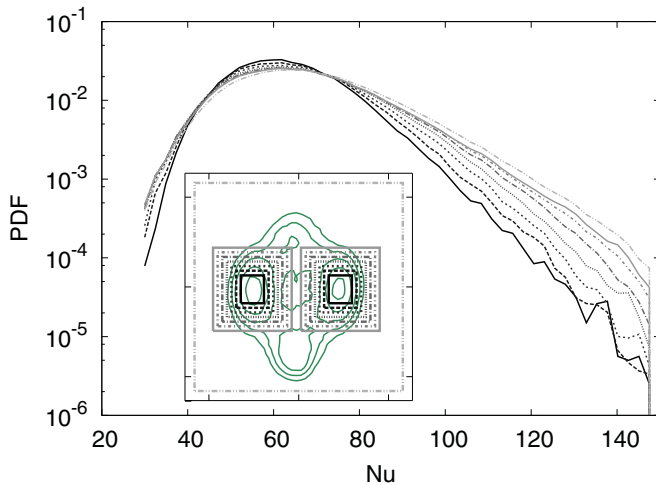


FIG. 10. (Color online) PDF of the Nusselt number conditioned on the one-cell pattern with varying threshold. The inset of this figure shows the contour map of the PDF from the 2D ξ_{11} , ξ_{21} state subspace (see Fig. 6), with the selected domains respective to this threshold; a systematic decline of the tail for higher Nusselt number values is visible for a decreasing area around the distinct maxima indicating the most probable configuration in state subspace.

Nusselt number PDF exhibits a more asymmetric behavior with exponential tails for values higher than the mean value. However, by increasing the threshold, the observed domain gets smaller, and there is a systematic transition to more symmetric PDFs. The tails for higher values decline, while the tails for smaller values remain more static.

VII. CONCLUSIONS

In this paper a statistical analysis of Rayleigh-Bénard convection in the infinite Prandtl regime has been presented with particular regard to reversals of the global flow pattern. By means of a global mode decomposition, we extract information about the stability and the statistical dependency with respect to different primary flow modes. We also connect these primary

modes with the Nusselt number of the corresponding flow fields in order to analyze which structures are transporting the most amount of heat through the fluid layer. The comparison between the temporal evolution of the vertical velocity at the side walls at middepth and a reduced model of a finite set of modes shows that the global dynamics can be characterized by at least two modes. Analysis of a generic reversal also indicates that the amplitudes ξ_{11} and ξ_{21} dominate the temporal evolution of the LSC. Due to statistical analysis in state subspace spanned by two predominant modes, we are able to extract the dependency between both modes as well as the reversal path in state subspace. Special attention has been given to the characterization of typical reversal sequences. Our study indicates, unlike previous work [13–16], that a generic mechanism always involves transitions over higher-order modes. Such a reversal goes along with a breakdown of the LSC through a strong interaction of plumes with the bulk, an excitation of higher flow modes, a breakdown of this partly stable flow pattern, and a reestablishment of a reversed LSC. Thus the present paper allows us to characterize the dynamics and the irregular reorientation of the LSC. The interaction between the small-scale structures in form of plumes with the bulk leads to an increased heat transport; however, due to the rare occurrence of the plumes they do not change the contribution to the heat transport significantly. Furthermore, a major issue for future research would be to analyze a different parameter range of Rayleigh number and aspect ratio Γ , to investigate which structures are dominating the global flow pattern. An important future challenge will be the connection between the primary modes and the governing equations in order to extract low-dimensional model equations to characterize the global dynamics of the flow field on the basis of the primary flow patterns.

ACKNOWLEDGMENTS

The work benefited from the constructive comments by the two anonymous referees. The authors also thank O. Kamps for helpful discussions within the framework of CeNoS.

-
- [1] G. Ahlers, S. Grossmann, and D. Lohse, *Rev. Mod. Phys.* **81**, 503 (2009).
 - [2] R. Krishnamurti and L. N. Howard, *Proc. Natl. Acad. Sci. USA* **78**, 1981 (1981).
 - [3] X. L. Qiu and P. Tong, *Phys. Rev. E* **64**, 036304 (2001).
 - [4] H. D. Xi, S. Lam, and K.-Q. Xia, *J. Fluid Mech.* **503**, 47 (2004).
 - [5] T. A. Hartlep, A. Tilgner, and F. H. Busse, *J. Fluid Mech.* **544**, 309 (2005).
 - [6] R. Verzicco and R. Camussi, *J. Fluid Mech.* **477**, 19 (2003).
 - [7] S. Cioni, S. Ciliberto, and J. Sommeria, *J. Fluid Mech.* **335**, 111 (1997).
 - [8] H. D. Xi and K.-Q. Xia, *Phys. Rev. E* **78**, 036326 (2008).
 - [9] E. Brown and G. Ahlers, *J. Fluid Mech.* **568**, 351 (2006).
 - [10] U. Hansen, D. A. Yuen, and S. E. Kroening, *Geophys. Astrophys. Fluid Dyn.* **63**, 67 (1992).
 - [11] M. Breuer and U. Hansen, *Europhys. Lett.* **86**, 24004 (2009).
 - [12] P. K. Mishra, A. K. De, M. K. Verma, and V. Eswaran, *J. Fluid Mech.* **668**, 480 (2011).
 - [13] F. F. Araujo, S. Grossmann, and D. Lohse, *Phys. Rev. Lett.* **95**, 084502 (2005).
 - [14] K. R. Sreenivasan, A. Bershadskii, and J. J. Niemela, *Phys. Rev. E* **65**, 056306 (2002).
 - [15] R. Benzi, *Phys. Rev. Lett.* **95**, 024502 (2005).
 - [16] E. Brown and G. Ahlers, *Phys. Fluids* **20**, 075101 (2008).
 - [17] G. Schubert, D. L. Turcotte, and P. Olson, *Mantle Convection in the Earth and Planets* (Cambridge University Press, Cambridge, 2001).
 - [18] J. Schmalzl, M. Breuer, and U. Hansen, *Europhys. Lett.* **67**, 390 (2004).
 - [19] S. Grossmann and D. Lohse, *J. Fluid Mech.* **407**, 27 (2000).
 - [20] S. Grossmann and D. Lohse, *Phys. Rev. Lett.* **86**, 3316 (2001).

- [21] K. Sugiyama, R. Ni, R. J. A. M. Stevens, T. S. Chan, S. Q. Zhou, H. D. Xi, C. Sun, S. Grossmann, K. Q. Xia, and D. Lohse, *Phys. Rev. Lett* **105**, 034503 (2010).
- [22] J. Boussinesq, *Théorie Analytique de la Chaleur*, Vol. 2 (Gauthier-Villars, Paris, 1903).
- [23] R. A. Trompert and U. Hansen, *Geophys. Astrophys. Fluid Dyn.* **83**, 261 (1996).
- [24] M. Breuer, S. Wessling, J. Schmalzl, and U. Hansen, *Phys. Rev. E* **69**, 026302 (2004).
- [25] J. Bailon-Cuba, M. S. Emran, and J. Schumacher, *J. Fluid Mech.* **655**, 152 (2010).
- [26] T. R. Smith, J. Moehlis, and P. Holmes, *Nonlinear Dyn.* **41**, 275 (2005).
- [27] R. Friedrich, J. Peinke, and M. R. R. Tabar, in *Encyclopedia of Complexity and Systems Science*, edited by R. A. Meyers (Springer, New York, 2009), p. 3574–3597.
- [28] H. D. Xi and K.-Q. Xia, *Phys. Fluids* **20**, 055104 (2008).
- [29] U. Hansen, D. A. Yuen, and A. V. Malevsky, *Phys. Rev. A* **46**, 4742 (1992).
- [30] J. Arkani-Hamed, *Nonlin. Proc. Geophys.* **4**, 19 (1997).
- [31] P. Olson and G. M. Corcos, *Geophys. J. R. Astron. Soc.* **62**, 195 (1980).